Check for updates

OPEN

# Large eddy simulation of turbidity currents in a narrow channel with different obstacle configurations

Danial Goodarzi[1]✉, Kaveh Sookhak Lari[2,3], Ehsan Khavasi[4] & Soroush Abolfathi[5]

Turbidity currents are frequently observed in natural and man-made environments, with the potential of adversely impacting the performance and functionality of hydraulic structures through sedimentation and reduction in storage capacity and an increased erosion. Construction of obstacles upstream of hydraulic structures is a common method of tackling adverse effects of turbidity currents. This paper numerically investigates the impacts of obstacle's height and geometrical shape on the settling of sediments and hydrodynamics of turbidity currents in a narrow channel. A robust numerical model based on LES method was developed and successfully validated against physical modelling measurements. This study modelled the effects of discretization of particles size distribution on sediment deposition and propagation in the channel. Two obstacles geometry including rectangle and triangle were studied with varying heights of 0.06, 0.10 and 0.15 m. The results show that increasing the obstacle height will reduce the magnitude of dense current velocity and sediment transport in narrow channels. It was also observed that the rectangular obstacles have more pronounced effects on obstructing the flow of turbidity current, leading to an increase in the sediment deposition and mitigating the impacts of turbidity currents.

Density currents, also known as gravity currents, are primarily horizontally moving fluid flow with higher densities than ambient flow, as a result of variations in temperature and concentration of dissolved and suspended particles[1]. In particular for the latter, currents with varying concentrations of suspended particles are also referred to as turbidity currents[2]. In turbidity currents, buoyancy-driven forces propagate the denser fluid into the ambient fluid with lower density. The suspension and deposition of sediments resulted by turbidity currents could limit the level of functionality and effectiveness of hydraulic structures by reduction in the storage capacity and an increased chance of erosion[3]. Turbidity currents are common in both natural (e.g., rivers) and man-made hydraulic systems (e.g., release of wastewater into a channel). Hence, understanding the characteristics and dynamics of turbidity currents is of great interest for engineers and scientists[4,5].

Release of a dense fluid into a lighter ambient fluid from a non-continues source (e.g., the lock-exchange technique) or a continuous source (e.g., a dense jet) has been studied in several experimental investigations[6–18]. Experimental investigations also assessed the interactions between turbidity currents of different densities and velocities with an obstacle of varying geometrical features including height and width[19–27]. Alexander et al. (1994) experimentally investigated the effects of the bed topography on the flow and accumulation of the sediment, by studying variations in the depth of the dense flow and velocity before reaching the obstacle[19]. The impacts of the obstacle's height on the blockage of the dense flow was studied by Woods et al. (1998). They concluded that an increase in the obstacle height can result in flow obstruction[28]. Morris et al. (2003) experimentally showed the influence of obstacles on the increase of thickness of the sedimentation layer at a considerable distance upstream of the obstacles[29]. Kubo (2004) explored the relationships between topographic features of a channel and particle deposition on ramps and humps in a series of experiments and numerical studies, concluding an increase in

[1]Department of Civil, Water and Environmental Engineering, Shahid Beheshti University, Tehran, Iran. [2]CSIRO Land and Water, Private Bag No. 5, Wembley, WA 6913, Australia. [3]School of Engineering, Edith Cowan University, 270 Joondalup Drive, Joondalup, WA 6027, Australia. [4]Department of Mechanical Engineering, University of Zanjan, Zanjan, Iran. [5]School of Engineering, The University of Warwick, Coventry CV4 7AL, UK. ✉email: danial.goodarzi@yahoo.com

particles deposition downstream of the downslope and on the upslope of the humps[30]. Oshaghi et al. (2013) demonstrated that the obstacle height and the upstream velocity of turbidity currents are inversely related[19]. Khavasi et al. (2012 and 2019) studied the effects of particle size, bed slope and inlet Froude number on the stability of turbidity currents. They demonstrated that an increase in the particles size, bed slope and inlet Froude number can diminish the stability of the dense flow regime[31–34].

Numerical approaches have also been used to study the dynamics of turbidity currents. Toniolo et al. (2007) developed a numerical framework to predict the trapping efficiency of turbidity currents in reservoirs and showed the impacts of topology on the reduction of fine particles settling efficiency[35]. Oehy et al. (2007) compared solid and porous obstacles confronting turbidity currents and showed a slight reduction in the trapping efficiency for porous obstacles[36].

Several turbulence models and simulation approaches have been used to study turbidity currents including Direct Numerical Simulation (DNS), Large Eddy Simulation (LES) and Reynolds-averaged Navier–Stokes equations (RANS). RANS turbulence models are less computationally expensive in comparison with LES and DNS. RANS models with k-ε turbulence closure have been used in several studies of turbidity currents[37–41]. However, RANS models usually fail to accurately resolve flow zones with intense shear (near walls or obstacles) and flow of low to moderate Reynolds number[42,43]. Additionally, the numerical constants in RANS models need careful tuning procedures for the specific flow conditions in order to improve the accuracy of the solution, given that the Reynolds stresses in the RANS equations depend on the boundary and flow conditions. In the LES models, filtered-out eddies are not influenced by the flow conditions as the governing equations are derived based on the physical properties of the flow[37,44]. This study, for the first time, develops a numerical simulation framework using an LES turbulence model to investigate turbidity currents confronting obstacles of various geometrical configurations in a narrow channel. Also, for the first time, this study investigates the effects of discretization of particles size distribution on sediment deposition and propagation in narrow channels. The flow hydrodynamics and sediment concentration of turbidity currents over two obstacles of varying geometrical configurations in a narrow channel are investigated using the validated method described in this paper. This study highlights the capabilities of the LES numerical approaches for robust and accurate prediction of turbidity currents.

## The model

A dense current occurs when a dense fluid propagates into a lighter fluid. The dense current is propagated under the combined influence of its initial momentum and the gravity body force[1] (Fig. 1). A lab-scale narrow channel containing freshwater is considered to investigate the behavior of turbidity currents. The choice of the narrow channel in this study is to characterize the augmented effects of the shear stress caused by side walls. A dense current is released into the channel and the interactions of the dense current with the fresh water (ambient) flow is simulated using LES model described in below.

Fluid flow is governed by the Navier–Stokes equations including continuity and momentum conservation equations. The concentration of particles in the dense current is modelled with a transport equation. The density difference between dense and light (ambient) fluids is assumed to be sufficiently low so that the Boussinesq approximation remains valid for modelling buoyancy forces. The gravity-buoyancy term in the momentum equation is defined as[45]:

$$(\rho - \rho_0)g = \rho_0\beta(C - C_0)g \tag{1}$$

where $C$ and $C_0$ represent the normalized particle concentrations [unit less] at density $\rho$ and $\rho_0$ [kg/m³] for the dense and ambient fluid, respectively. The volumetric coefficient of expansion for the particles is $\beta = 1$ [dimensionless] and $g$ represents the gravitational acceleration [m/s²]. In this study,$C$ varies from $C_0 = 0$ to $C_{max} = 1$. To conduct a Large Eddy Simulation (LES), the continuity and momentum conservation equations are defined as:

$$\frac{\partial \overline{U_i}}{\partial x_i} = 0 \tag{2}$$

$$\frac{\partial \overline{U_i}}{\partial t} + \frac{\partial \overline{U_i U_j}}{\partial x_i} = -\frac{\partial \overline{p}}{\partial x_i} + \frac{\partial}{\partial x_j}\left(\frac{1}{Re_b}\frac{\partial \overline{U_i}}{\partial x_j}\right) - \frac{\partial \tau_{ij}}{\partial x_j} + \overline{C}e_i^g \tag{3}$$

where $\bar{U}$ represents the filtered velocity [m/s], $t$ is the time [s], $e_i^g$ denotes the unit vector pointing in the direction of gravity and $\bar{p}$ is the filtered pressure [kg/m s²][36,46–50]. Reynolds number in this system $Re_b$ is determined based on the buoyancy velocity ($U_b$):

$$U_b = \sqrt{H_{inlet} \times g\frac{\rho - \rho_0}{\rho_0}} \tag{4}$$

$$Re_b = \left(\frac{U_b H_{inlet}}{\nu}\right) \tag{5}$$

where $\nu$ is the kinematic viscosity [m²/s] and $H_{inlet}$ denotes the height of dense fluid at the inlet [m]. The ratio of the kinematic viscosity $\nu$ to the diffusion coefficient of suspended particles $D$ [m²/s] is known as the Schmidt number (Sc). The length scales are computed by the Batchelor scale $\lambda_B$ [m] showing the smallest scale for a diffusing scalar. The $\lambda_B$ is defined as the ratio of the Kolmogorov length scale $\eta$ [m] to the square root of the Schmidt number $Sc$ as[44]:
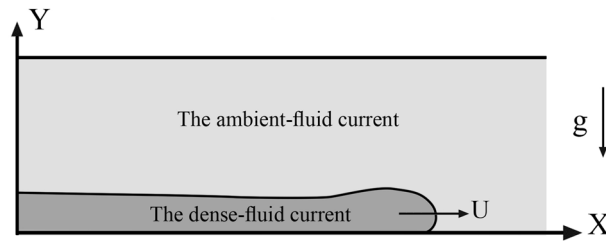
**Figure 1.** Schematic description of a dense current problem.

$$\eta = \left(\frac{\upsilon^3}{\varepsilon}\right)^{1/4} \tag{6}$$

$$\lambda_B = \frac{\eta}{\sqrt{Sc}} \tag{7}$$

where $\varepsilon$ is the local dissipation rate of the turbulent kinetic energy [m²/s³]. In order to simulate the smallest diffusive scales, high resolution mesh is required, which significantly increases the computational costs. The previous studies have reported that $Sc \geq 1$ has no remarkable effects on the computational accuracy[44,49,51–54]. In this study, to maintain reasonable computational costs, the Schmidt number is assumed to be $Sc = 1$.

The particles inertia forces and particle–particle interactions are not computed as the concentration of suspended solids is relatively low[52,55]. Therefore, particle's transport is simultaneously governed by the flow hydrodynamic and Stokes' settling velocity[56]:

$$U_s = \frac{d_p^2(\rho_p - \rho)g}{18\mu} \tag{8}$$

where $\mu$ is the dynamic viscosity [kg/m.s], $d_p$ denotes the diameter of particles and $\rho_p$ is the density of particles [kg/m³]. Ten different particle size intervals ranging from 0.5–100 μm are considered to represent the particles with an identical density $\rho_p$. For each particle size, the Eulerian continuum transport equation is implemented according to Eq. (9)[57], with a constant value for the Stokes' settling velocity $U_s$:

$$\frac{\partial \overline{C_i}}{\partial t} + \frac{\partial \overline{(U_i + U_s)C_i}}{\partial x_i} = \frac{\partial}{\partial x_i}\left(\frac{1}{ScRe_b}\frac{\partial \overline{C_i}}{\partial x_i}\right) - \frac{\partial \tau_i^C}{\partial x_i} \tag{9}$$

Effects of the filtered fluctuations of the flow hydrodynamic are considered by the momentum and concentration residual-stress tensors $\tau_{ij}$ and $\tau_i^C$:

$$\tau_{ij} = \overline{U_i U_j} - \overline{U_i}\,\overline{U_j} \tag{10}$$

$$\tau_i^C = \overline{CU_i} - \overline{C}\,\overline{U_i} \tag{11}$$

Turbulence effects are modelled using Smagorinsky closure model[58], including a SGS eddy-viscosity $\upsilon_{SGS}$ model to compute the residual tensors:

$$\tau_{ij} = -2\upsilon_{SGS}\overline{S_{ij}} \tag{12}$$

$$\upsilon_{SGS} = (C_s\Delta)^2\sqrt{\overline{S_{ij}S_{ij}}} \tag{13}$$

$$\overline{S_{ij}} = \frac{1}{2}\left(\frac{\partial \overline{U_i}}{\partial \overline{x_j}} + \frac{\partial \overline{U_j}}{\partial \overline{x_i}}\right) \tag{14}$$

where $\overline{S_{ij}}$ is the strain tensor, Smagorinsky coefficient is taken as $C_s = 0.2$, $\Delta$ denotes the filtered width and turbulent Schmidt number (which is from the order of unity[59,60]) is taken as 1. The computational domain is set up in a three-dimensional Cartesian coordinate system including rectangular channel 12 m long, 0.2 m wide and 0.6 m deep, based on Farizan et al. (2018) experimental investigations[61]. The numerical flume is then utilized to investigate the hydrodynamic behaviour of turbidity current on a sloping bed subjected to different obstacles configurations. The channel bed is assumed to be smooth with a slope of 1% (Fig. 2). A continuous dense current introduced into the channel, with a constant particle density $\rho = 2649\left(kg/m^3\right)$ and a mean diameter $D_{50} = 11\mu m$.
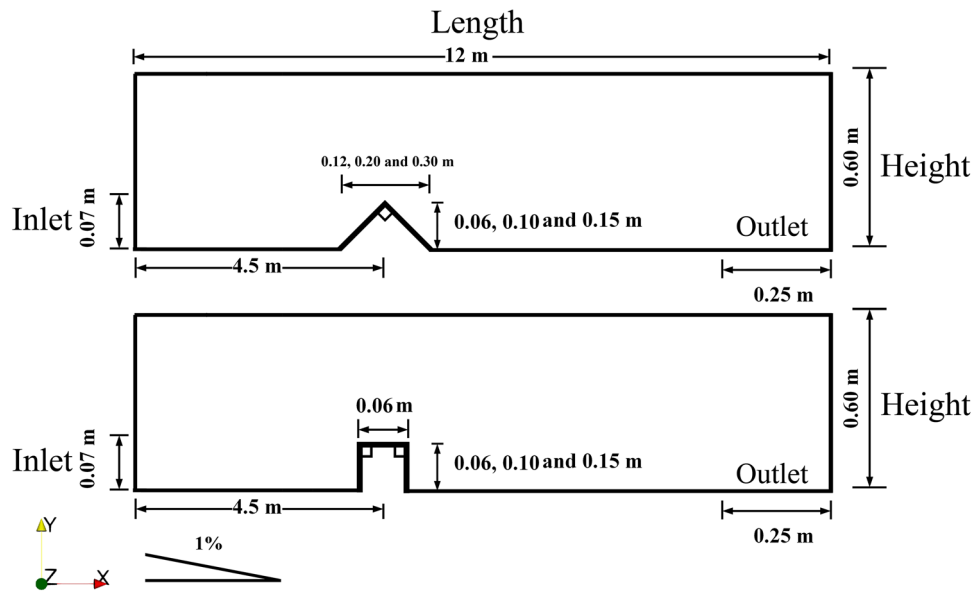
**Figure 2.** Schematic of the numerical domain and channel geometry with rectangular and triangular obstacles (subfigures are not drawn to scale).

| Case | Inlet densimetric Froude number | Inlet concentration (kg/m³) | Height of the obstacle (cm) | Type of obstacle |
|------|---------------------------------|------------------------------|------------------------------|------------------|
| 1 | 0.8 | 6.75 | 6 | Triangle |
| 2 | 0.8 | 6.75 | 10 | Triangle |
| 3 | 0.8 | 6.75 | 15 | Triangle |
| 4 | 0.8 | 6.75 | 6 | Rectangle |
| 5 | 0.8 | 6.75 | 10 | Rectangle |
| 6 | 0.8 | 6.75 | 15 | Rectangle |

**Table 1.** Summary of simulation scenarios.

Two obstacle configurations with triangular and rectangular geometries were tested in this study. The effects of obstacle's height on the turbidity current were investigated by three different obstacle's height of 0.06 m, 0.10 m and 0.15 m. The obstacles were located 4.5 m downstream of the inlet to minimize effects of the inlet boundaries on the particles settling rate. The inlet flow densimetric Froude number Eq. (15) was set to 0.8 for all simulation cases, ensuring a sub-critical flow condition.

$$F_{inlet} = \frac{U_0}{\sqrt{g'H_{inlet}cos\theta}} \tag{15}$$

where $U_0$ is the mean velocity of the turbidity current at the inlet, $H_{inlet}$ is the height of the inlet and the bottom slope is $\theta$. The reduced gravity acceleration is determined as[61]:

$$g' = \frac{g(\rho - \rho_0)}{\rho_0} \tag{16}$$

where $\rho$ and $\rho_0$ are density of the turbidity current and the ambient fluid, respectively.

Six simulation scenarios are designed to determine the effects of obstacles height and geometrical shape on the behavior of turbidity currents. A summary of simulation cases is shown in Table 1.

To guarantee an appropriate determination of the turbulent boundary layer, the first grid cell adjacent to the solid boundary is resided in the viscous sub-layer ($y^+ < 5$) for a robust resolve of the boundary layer[50]. The location of this grid cell in plus units and associated parameters are described by Eqs. (17–20)[62,63]:

$$\frac{U_1}{U_\tau} = y^+ \tag{17}$$

$$y^+ = \frac{U_\tau \Delta y}{\upsilon} \tag{18}$$

4

$$U_\tau = \sqrt{\frac{\tau_w}{\rho}} \qquad (19)$$

$$\tau_w = \mu \frac{\partial U}{\partial y} \qquad (20)$$

where $y^+$ is the dimensionless distance from the wall, $U_1$ represents the velocity at the first cell, $\Delta y$ is the distance of the first cell from the solid boundary, $\tau_w$ and $U_\tau$ are wall shear-stress [kg/m·s$^2$] and associated friction velocity, respectively[64]. The height of the first cell was determined using the well-established empirical correlations described by Eqs. (21–23)[50,62,63]:

$$\tau_w = \frac{1}{2} c_f \rho U^2 \qquad (21)$$

$$c_f = 0.0577 Re_x^{-1/5} \qquad (22)$$

$$Re_x = \frac{U_x}{\upsilon} \qquad (23)$$

where $c_f$ is the wall skin friction coefficient, $Re_x$ denotes the Reynolds number based on the boundary layer thickness, $U_x$ is the inlet velocity [m/s] and $c_f$ is an empirical constant computed based on Reynolds number described by Eq. (23).

## Model verification

The numerical model was developed using finite-volume technique and computational codes were written in C++ with OpenFOAM (V6) open-source license. Second-order limited linear scheme was implemented for discretizing governing equations, except for the transport equation where a second-order QUICK scheme was adopted. The numerical robustness and accuracy of the QUICK scheme have been demonstrated by previous related studies[46–48,51]. The Pressure Implicit with Splitting of Operators (PISO) algorithm was implemented to solve the filtered LES equations in a transient mode. A two-steps corrector was considered in the PISO algorithm to guarantee computational robustness and a better convergence (i.e. pressure equation is corrected two times per time-step to satisfy the continuity equation)[65–67]. A series of numerical simulations were conducted to verify the numerical method and the developed model.

In turbidity currents, where complex phase-coupling (momentum exchange) between particles and fluid exists, velocity profiles determines the sediment deposition and the characteristics of flow hydrodynamic. A common method to evaluate the performance of numerical methods and computational codes is comparing the numerical results with physical modelling measurements[36,47,68–74]. Comparison of vertical variations of the numerical velocity profiles with the experimental measurements of Farizan et al. (2018) was conducted to validate the numerical model described in[61].

The temporally-averaged velocity profiles at 0.5 m before the obstacle were obtained once the steady-state condition is reached, and then are compared with the experimental measurements of Farizan et al.[61]. For the validation case, channel (L:12 m, W: 0.2 m and H: 0.6 m) with a triangle obstacle located at 4.5 m away from the inlet was considered. The inlet geometry has the same width as the channel (= 0.2 m) with the height of 0.07 m. A fully developed flow condition is applied at the inlet for the turbidity current entering into the channel to include turbulent flow fluctuations. Three grid resolutions with 3.900, 4.350 and 5.590 million structured hexahedron cells (namely Mesh 1, Mesh 2 and Mesh 3, respectively) were considered along with a mean particle diameter of $D_{50} = 11 \mu m$, to conduct sensitivity analysis and mesh dependency study. Time-averaged velocity profiles at a distance of 4 m from the inlet were determined for the validation test cases (Mesh 1, Mesh 2 and Mesh 3) with one concentration transport equation, and compared with the laboratory measurements of Farizan et al.[61] (Fig. 3). The comparison of the results presented in Fig. 3 highlights considerable deviations between experimental and numerical velocity profiles. The numerical model with one concentration transport equation overestimates the shear effects in the dense current and the velocity profile near the bed (the lower part of the velocity profile). It was shown that by ignoring the particles larger than $D_{50}$, the velocity of turbidity current near the bed was increased.

To improve the discrepancy between numerical results and the measurements, additional concentration transport equations were considered. Additional simulation cases with two, five and ten concentration transport equations were conducted to produce a more robust estimation of the particles size and distribution (0.5–100 μm). Figure 4 shows the distribution of particles experimentally measured by Farizan et al. (2018)[61].

Figure 5 compares the velocity profiles from numerical simulations with the experimental measurements of Farizan et al. (2018)[61]. The simulation sets presented in Fig. 5 include extra particle size intervals and more transport equations to enhance the computational accuracy of the velocity profiles. The simulations show that for all the cases, the velocity in the upper region of the turbidity current (see Fig. 6) is increased as finer particles are introduced to the flow, while the lower region of the turbidity current (near the channel bed) is slowed down due to the effects of larger particles. The accuracy of the numerical results is improved by increasing the number of concentration transport equations and the best performance was achieved for the case of 10 concentration transport equations. Following grid dependency analysis, to achieve numerical stability, computational
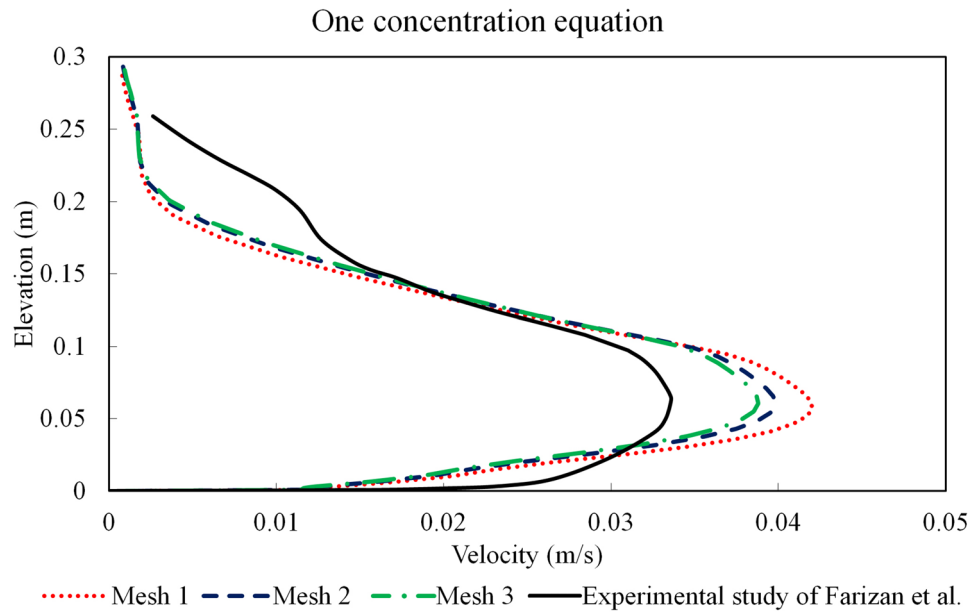
## One concentration equation



**Figure 3.** Comparison of the numerical and physical modelling of velocity profiles for the turbidity current with one concentration equation at x = 4 m (0.5 m upstream of the obstacle) for triangular obstacle (case 1).
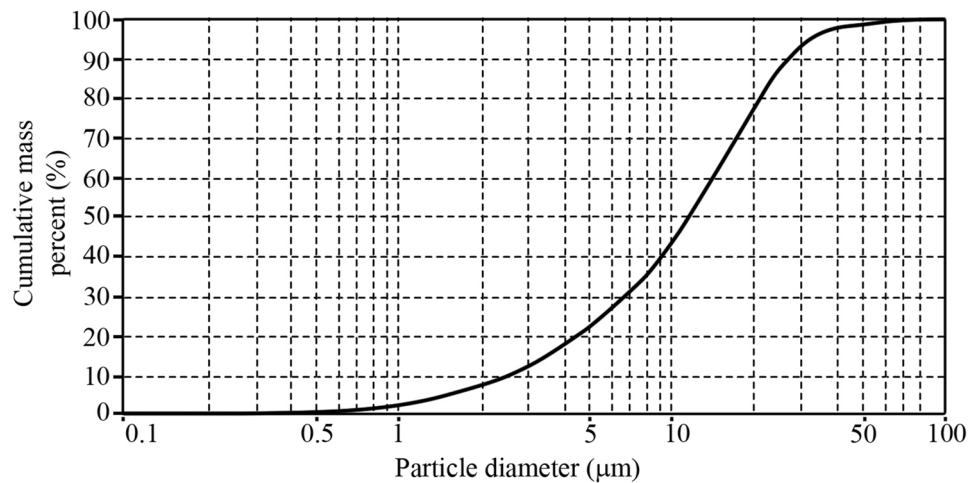


**Figure 4.** Particle diameter distribution in this study. Adopted from Farizan et al. (2018)[61].

accuracy and cost-effective solution, Mesh 2 with 4.350 million structured hexahedron cells was selected for further simulations.

Despite the shear stress effects of walls on the fluid might initially seem to be significant, in this narrow channel, the results showed that at the Reynolds number considered in this study the walls effect is negligible, which is in good agreement with the study by Khavasi et al. and Oehy et al.[31,32,36,68].

## Results and discussion

The velocity and concentration profiles inside the dense layer of the turbidity current are categorized into three distinct regions (Fig. 6): (1) the upper part is known as a shear layer region where the density of the turbidity current decreases and asymptotes to the counterpart value for the ambient fluid; (2) the middle part is known as the suspension zone where the majority of particles are suspended in the fluid; and (3) the lower zone which is a depositional area where particles are settled[31]. In this paper, the upper zone of the channel (part 1 in Fig. 6) is not described as the flow velocity asymptotes to zero[61].

Velocity and concentration values are measured after reaching a quasi steady-state to avoid temporal fluctuations in the flow parameters.
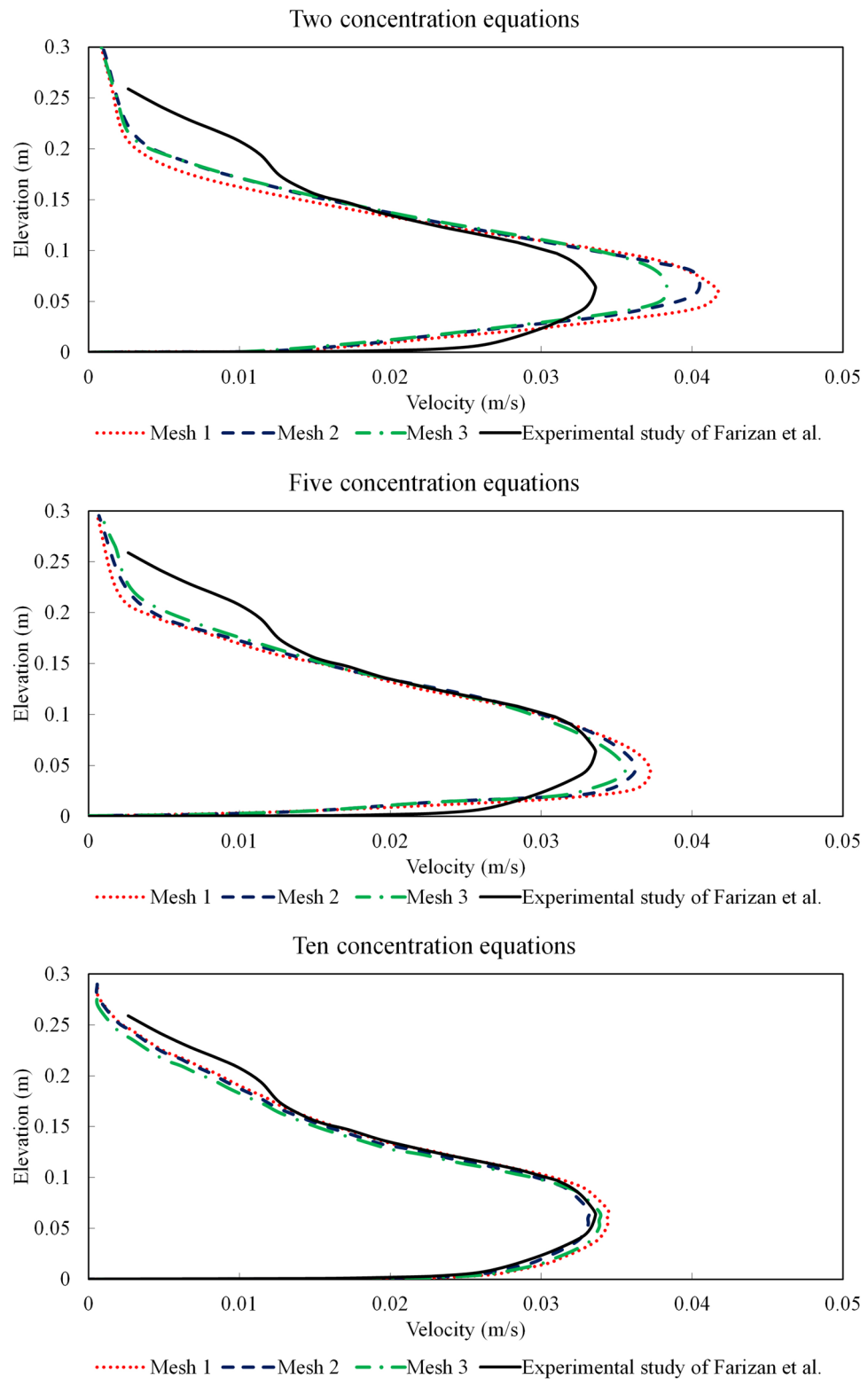
**Figure 5.** Comparison of the numerical and physical modelling of velocity profiles for the turbidity current with two, five and ten concentration equations at x = 4 m (0.5 m upstream of the obstacle) for triangular obstacle (Case 1).
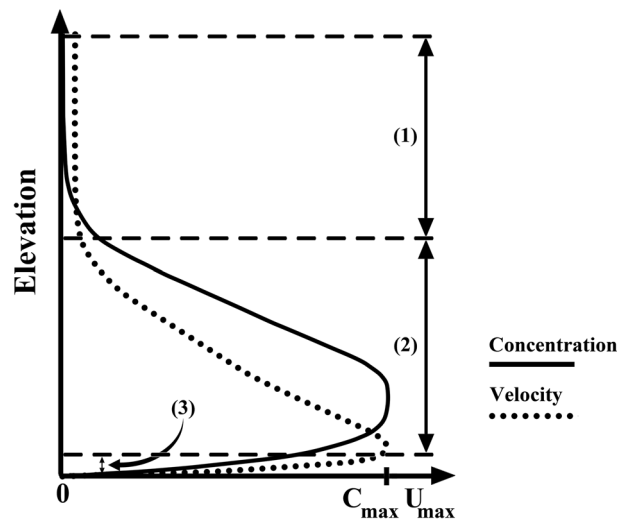
**Figure 6.** Schematic of the velocity and concentration profiles of turbidity currents[31].

Sediment deposition and entrainment rates are computed by measuring the vertical sediment flux and variations in the concentration of particles along the length of the channel. Suspended sediment flux per unit width is determined using Eq. (24) as:

$$q_s = \sum_0^{z_{upper}} u(z)c(z)\Delta z \quad (4)$$

(24)

where $z_{upper}$ is the upper boundary over which the concentration becomes negligible, $u(z)$ is the sum of settling and horizontal velocity and $c(z)$ is the concentration for the dense current.

The turbidity bore is defined as a moving hydraulic jump over the bed of the channel. Obstacles alter the flow regime and can move the internal bores towards the inlet of the channel. Also, the flow hydrodynamic characteristics significantly impact the position and structure of turbidity currents on the channel bed[36,75]. Figures 7 and 8 show temporal evolution of the turbidity current in the channel, indicating multiple reflected bores of the turbidity current as it travels inside the channel and over the obstacle. The horizontal velocity of turbidity current slightly decreases when the flow climbs up the obstacle which is due to the flow-obstacle interactions and the consequent dissipation of turbulent kinetic energy of the current (Figs. 7, 8). The bore of the dense flow becomes thinner immediately after it passes the obstacle and as it moves towards the outlet. For the case of both obstacles (Figs. 7, 8) sediment deposition and formation of an interface between turbidity current and the fluid of lighter density is observed[36].

Simulations were continued until the sediment deposition behind the obstacle reached a steady height. Temporally-averaged flow characteristics were determined once the quasi steady-state condition is met, to avoid temporal fluctuations of the LES.

The comparison between Figs. 7 and 8 at $t = 125$ s demonstrates an intensified turbulent hydraulic jump when the turbidity current passes over the rectangular obstacle. However, the flow over the triangular obstacle can be characterize as a quasi-uniform jump with a less disturbed flow.

Turbidity currents can significantly be influenced by the height of the obstacle. Previous studies show the effects of the obstacle on blockage and reflection of turbidity currents[36,61]. The obstacle's height of equal to twice the height of the current, was reported to cause a considerable reflection in the turbidity current flow[76].

Considering different heights, the stream-wise time-averaged velocity profiles of turbidity current in the quasi steady-state were plotted at 0.5 m upstream of both rectangular and triangular obstacles (Fig. 9). The increase in the height of the obstacles considerably changed the vertical structure of the dense current's velocity profiles. For the case of obstacle height of 0.06 m and for both geometries, the maximum velocity was observed in the settling zone behind the obstacle. For the cases with the obstacle height of 0.10 m, the velocity profile shows a sharp increase from the bottom up to the depth of 0.10 m, then a sharp reduction is seen up to the interface between the dense and ambient fluid. For the cases with the obstacle height of 0.15 m, the velocity profiles and vertical distribution of shear effects have smaller values with a less distributed pattern in comparison to the cases with smaller obstacle height. The patterns of the velocity profiles for both obstacles geometries are very similar, with the maximum velocities for the rectangular obstacle occurring at slightly higher depths from the bed. Rapid changes in the velocity profile of the turbidity current for the rectangular obstacle begin in higher elevation in contrast with triangular obstacle, which is due to the higher sediment decomposition for rectangular obstacle case.

Figure 10 shows the suspended sediment concentration inside the turbidity current upstream of the obstacle at 4 m from the inlet. The thickness and average concentration of the turbidity current upstream of the obstacle is increased with the increase in the height of the obstacles. The figure shows a thicker cloud of deposition for
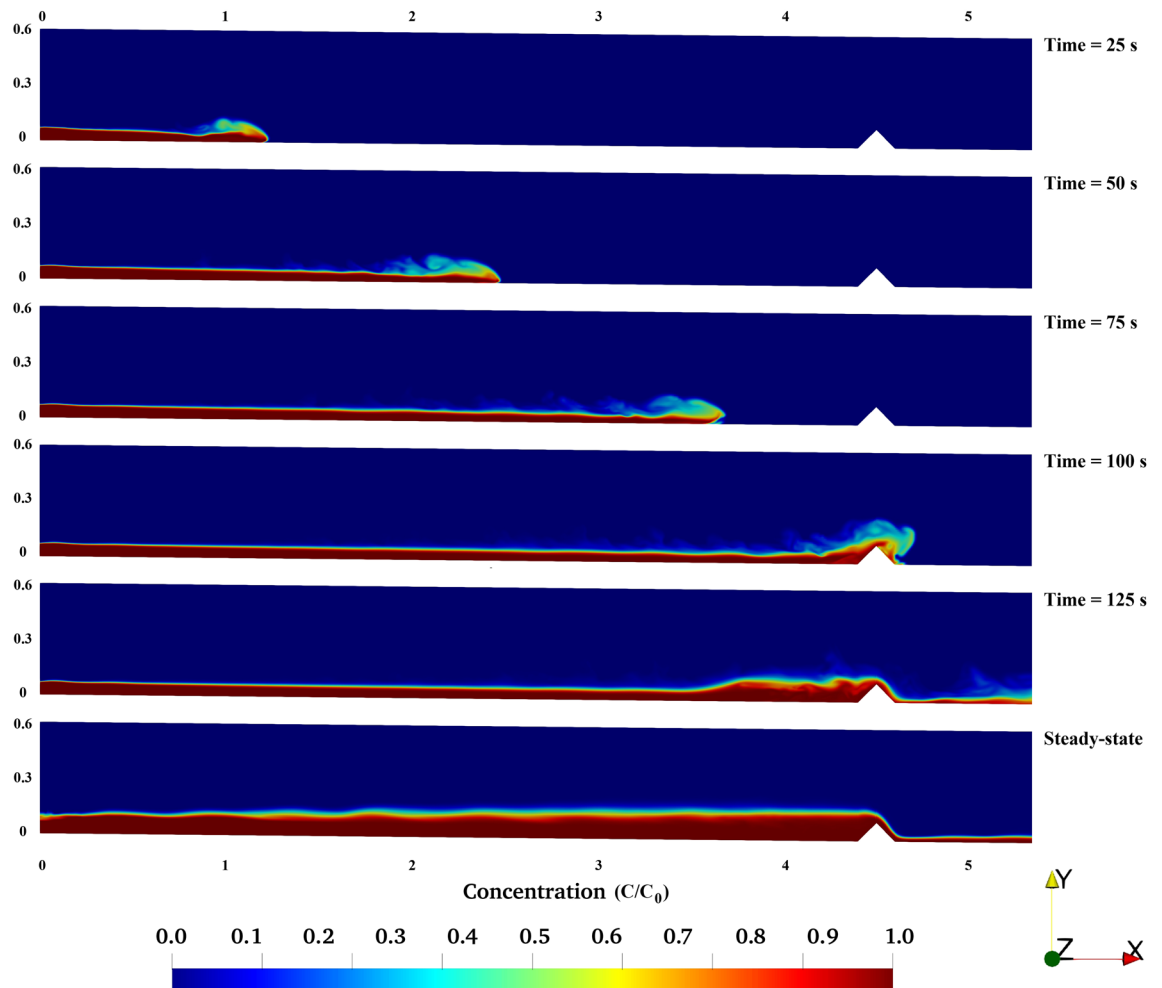
**Figure 7.** Simulation results for turbidity current flowing over triangular obstacle.

turbidity current behind the rectangular obstacle in comparison with the triangular obstacle, highlighting the effects of obstacle's geometrical shape on the control and mitigation of turbidity currents.

Figure 11 shows the suspended sediments flux per unit width of the channel for all the simulation cases. Implementation of the obstacles improved the settling efficiency for the turbidity current upstream of the obstacles. Increasing the height of the obstacles slowed down the vertical variation of horizontal velocity profile which led to a reduction in the sediment flux. The presence of obstacle, regardless of its geometrical shape, had no considerable impact on the settling rate at the downstream of the channel. The settling deposition of particles for the cases with 0.10 m and 0.15 m obstacles in the upstream of the obstacles are almost equal.

The effects of the obstacle's geometrical shape on the sediment deposition was more pronounced for the rectangular obstacles, mainly due to the higher reduction in the dense flow velocity behind the rectangular obstacle. In order to compare the obstacles shape impact, the difference in sedimentation flux-rate ($q_s$) for triangular and rectangular obstacles are determined (Table 2). Positive values indicate a dominancy in the settling of suspended sediments for the rectangular obstacle. Accordingly, rectangular obstacles are suggested to be implemented in channels leading to hydraulic control structures. More deposition of the sediments increases the efficiency of hydraulic structures in water systems[44].

$$q_{s\_variation} = \left( \frac{q_{s(triangular\,obstacle)} - q_{s(rectangular\,obstacle)}}{q_{s(triangular\,obstacle)}} \right) \times 100 \tag{25}$$

| X (m) | H = 6 cm (%) | H = 10 cm (%) | H = 15 cm (%) |
|-------|--------------|---------------|---------------|
| 4 | 3.38 | 4.76 | 10.1 |
| 4.5 | 1.14 | 1.54 | 3.47 |
| 5 | 0.98 | 1.02 | 2.34 |
| 5.5 | 0 | 0.98 | 1.57 |
| 6 | 0 | 0.4 | 0.97 |
| 6.5 | 0 | 0 | 0 |
| 7 | 0 | 0 | 0 |
| 7.5 | 0 | 0 | 0 |

**Table 2.** Sediment flux variation Eq. (25).
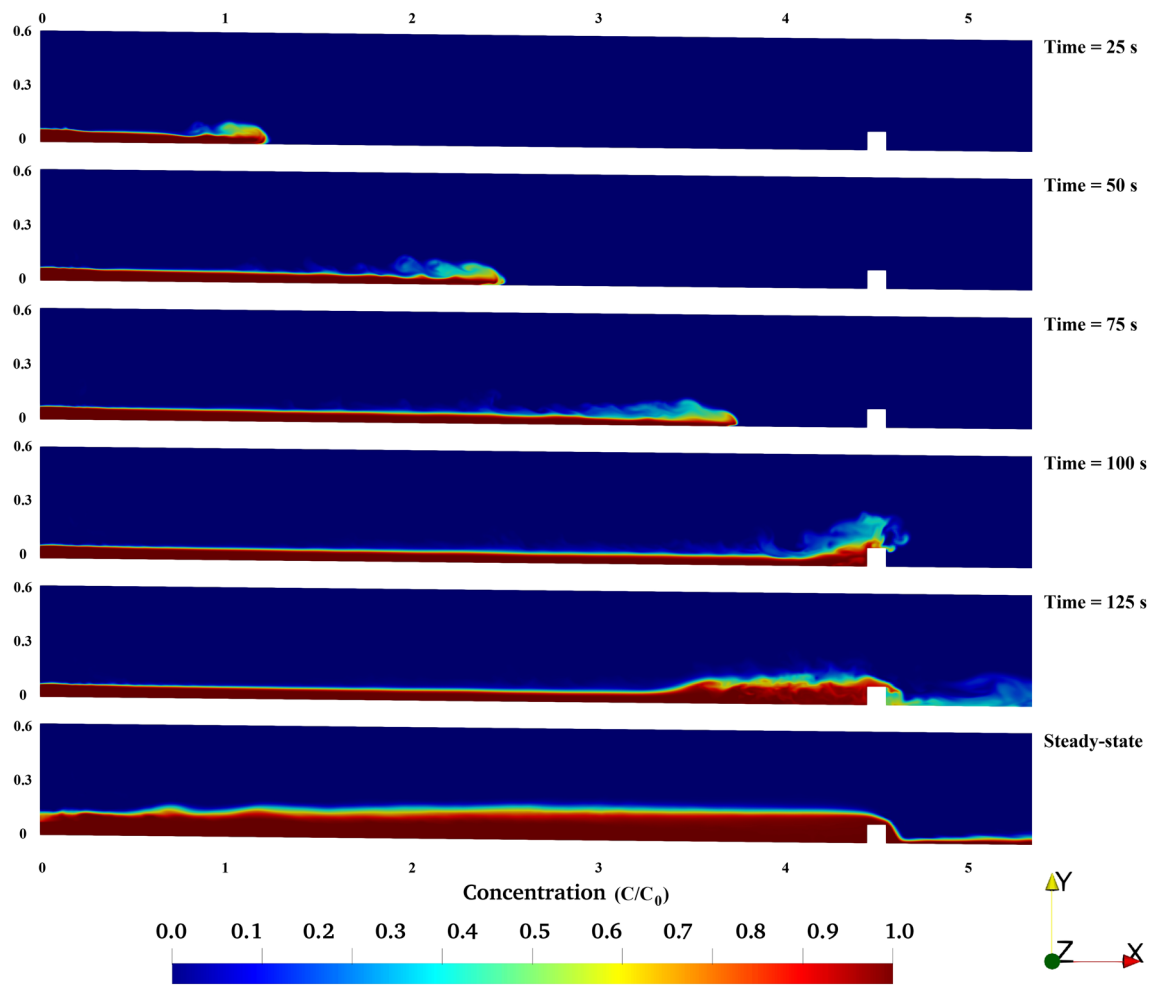


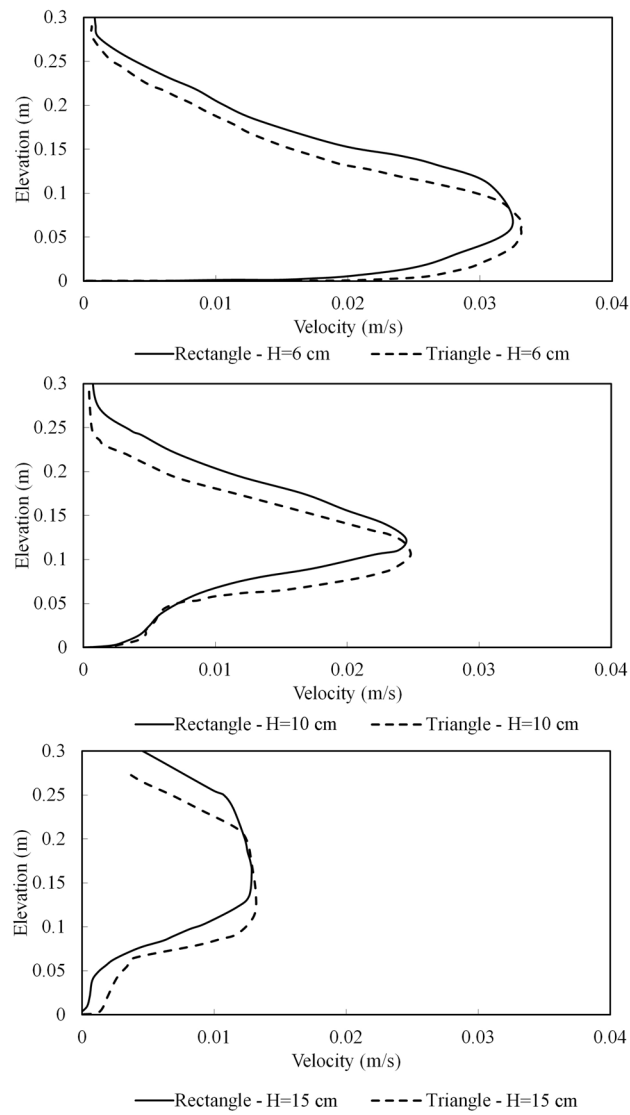**Figure 8.** Simulation results for turbidity current flowing over rectangular obstacle.

**Figure 9.** Velocity profiles of the turbidity current at x = 4 m for triangular and rectangular obstacles.
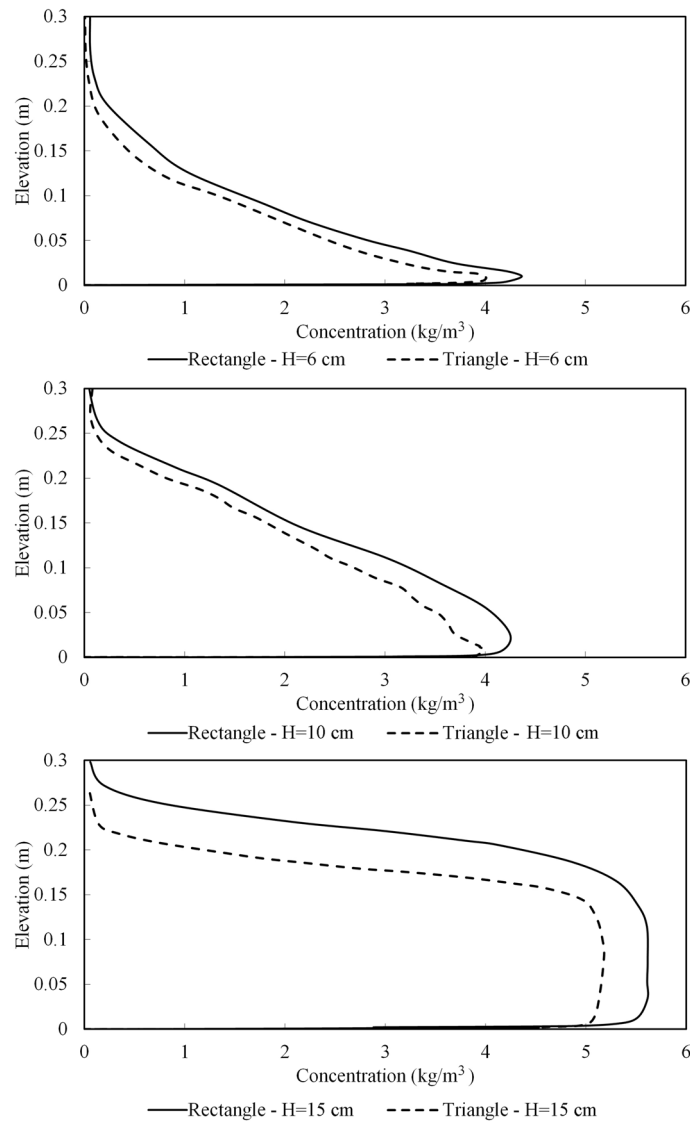
**Figure 10.** Concentration profiles of the turbidity current at x = 4 m for triangular and rectangular obstacles.
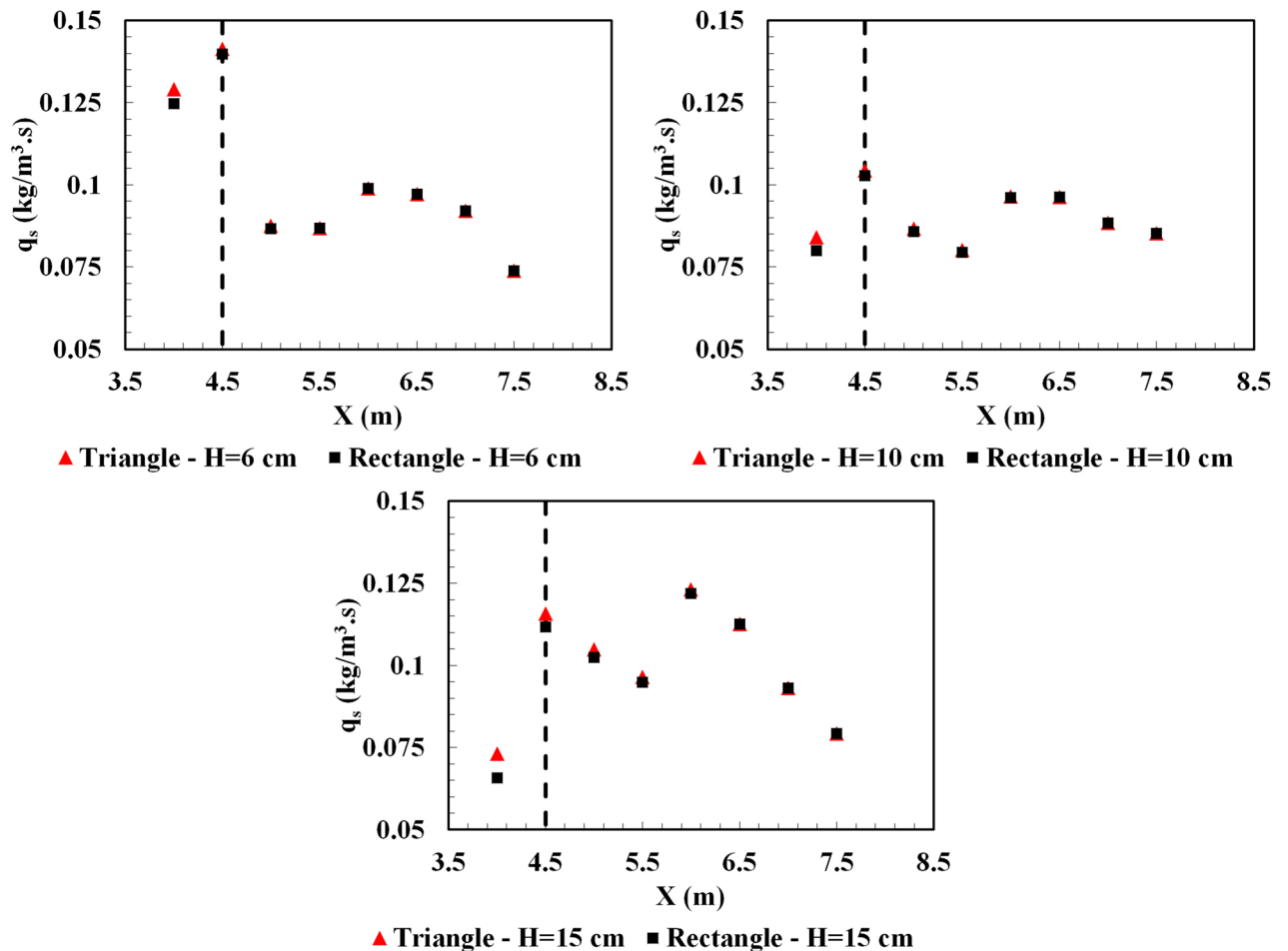
**Figure 11.** Sediment flux per unit width along the channel for all the simulation cases (dash lines show the location of obstacle).

## Conclusion

Appropriate understanding and analysis of turbidity currents are vital for sustainable and efficient management and operation of natural and man-made hydraulic structures. This study develops and successfully validates a high-resolution numerical simulation model using mathematical capabilities of Large Eddy Simulation (LES) technique. The effects of the number of concentration transport equations on the robustness and numerical accuracy were studied in detail. The results highlight that discretization of the particles size distribution improves the accuracy of the model in predicting turbidity current hydrodynamics and spatiotemporal structure of turbulence.

The effects of obstacle's geometrical shape and height on the turbidity currents characteristics in a narrow three-dimensional channel were modelled. Two obstacle prototypes of rectangular and triangular shape with varying height were investigated. The numerical velocity and concentration profiles were determined for all simulation cases described in Table1.

The findings indicate that, for both rectangular and triangular obstacles, by increasing the height of the obstacle, the maximum velocity of the turbidity current was reduced and the shape of the vertical distribution of flow hydrodynamic in the dense layer was changed. The results show that the increased height of obstacle directly impacted the vertical structure of shear and turbulent velocity. Across all test cases, comparison between the two obstacle geometries shows that for both obstacles the overall shapes of flow hydrodynamics are similar.

Furthermore, a direct relationship between the obstacle's height and the settling capability of the obstacles was observed. The numerical results highlight that the shape and height of obstacles significantly change the hydrodynamics, sediment particle distributions and structure of turbidity currents over a smooth bed channel. Installation of a rectangular obstacle is recommended to enhance the deposition and efficiency of hydraulic structures (dams, reservoirs and weirs) in water systems.

The computational framework developed in this study demonstrates that LES modelling can be implemented as computationally robust and reliable numerical technique to investigate the dynamics of turbidity currents in turbulent flow conditions.

## Data Availability

## References

1. Ungarish, M. *An introduction to gravity currents and intrusions*. (Chapman and Hall/CRC, 2009).
2. Lowe, D. R. Sediment gravity flows; II, Depositional models with special reference to the deposits of high-density turbidity currents. *J. Sediment. Res.* **52**, 279–297. https://doi.org/10.1306/212F7F31-2B24-11D7-8648000102C1865D (1982).
3. Thorpe, S. Gravity currents in the environment and the laboratory. *J. Fluid Mech.* **352**, 374–378. https://doi.org/10.1017/S0022112097227527 (1997).
4. Meiburg, E. & Kneller, B. Turbidity currents and their deposits. *Annu. Rev. Fluid Mech.* **42**, 135–156. https://doi.org/10.1146/annurev-fluid-121108-145618 (2010).
5. Pilskaln, C. H., Churchill, J. H. & Mayer, L. M. Resuspension of sediment by bottom trawling in the Gulf of Maine and potential geochemical consequences. *Conserv. Biol.* **12**, 1223–1229. https://doi.org/10.1046/j.1523-1739.1998.0120061223.x (1998).
6. Cenedese, C. & Adduce, C. Mixing in a density-driven current flowing down a slope in a rotating fluid. *J. Fluid Mech.* **604**, 369–388. https://doi.org/10.1017/S0022112008001237 (2008).
7. Laanearu, J., Cuthbertson, A. J. & Davies, P. A. Dynamics of dense gravity currents and mixing in an up-sloping and converging vee-shaped channel. *J. Hydraul. Res.* **52**, 67–80. https://doi.org/10.1080/00221686.2013.841779 (2014).
8. Gildeh, H. K., Mohammadian, A., Nistor, I. & Qiblawey, H. Numerical modeling of 30 and 45 inclined dense turbulent jets in stationary ambient. *Environ. Fluid Mech.* **15**, 537–562. https://doi.org/10.1007/s10652-014-9372-1 (2015).
9. Kheirkhah Gildeh, H., Mohammadian, A., Nistor, I. & Qiblawey, H. Numerical modeling of turbulent buoyant wall jets in stationary ambient water. *J. Hydraul. Eng.* **140**, 04014012. https://doi.org/10.1061/(ASCE)HY.1943-7900.0000871 (2014).
10. Inghilesi, R., Adduce, C., Lombardi, V., Roman, F. & Armenio, V. Axisymmetric three-dimensional gravity currents generated by lock exchange. *J. Fluid Mech.* **851**, 507–544. https://doi.org/10.1017/jfm.2018.500 (2018).
11. Lombardi, V., Adduce, C. & La Rocca, M. Unconfined lock-exchange gravity currents with variable lock width: laboratory experiments and shallow-water simulations. *J. Hydraul. Res.* **56**, 399–411. https://doi.org/10.1080/00221686.2017.1372817 (2018).
12. Ottolenghi, L., Prestininzi, P., Montessori, A., Adduce, C. & La Rocca, M. Lattice Boltzmann simulations of gravity currents. *European Journal of Mechanics-B/Fluids* **67**, 125–136. https://doi.org/10.1016/j.euromechflu.2017.09.003 (2018).
13. Kyrousi, F. *et al.* Large Eddy Simulations of sediment entrainment induced by a lock-exchange gravity current. *Adv. Water Resour.* **114**, 102–118. https://doi.org/10.1016/j.advwatres.2018.02.002 (2018).
14. Pérez-Díaz, B., Palomar, P., Castanedo, S. & Álvarez, A. PIV-PLIF characterization of nonconfined saline density currents under different flow conditions. *J. Hydraul. Eng.* **144**, 04018063. https://doi.org/10.1061/(ASCE)HY.1943-7900.0001511 (2018).
15. Pérez-Díaz, B., Castanedo, S., Palomar, P., Henno, F. & Wood, M. Modeling nonconfined density currents using 3D hydrodynamic models. *J. Hydraul. Eng.* **145**, 04018088. https://doi.org/10.1061/(ASCE)HY.1943-7900.0001563 (2019).
16. Zhao, L. *et al.* Front velocity and front location of lock-exchange gravity currents descending a slope in a linearly stratified environment. *J. Hydraul. Eng.* **144**, 04018068. https://doi.org/10.1061/(ASCE)HY.1943-7900.0001536 (2018).
17. Venuleo, S., Pokrajac, D., Schleiss, A. J. & Franca, M. J. Continuously-fed gravity currents propagating over a finite porous substrate. *Phys. Fluids* **31**, 126601. https://doi.org/10.1063/1.5124955 (2019).
18. De Falco, M., Ottolenghi, L. & Adduce, C. Dynamics of gravity currents flowing up a slope and implications for entrainment. *J. Hydraul. Eng.* **146**, 04020011. https://doi.org/10.1061/(ASCE)HY.1943-7900.0001709 (2020).
19. Alexander, J. & Morris, S. Observations on experimental, nonchannelized, high-concentration turbidity currents and variations in deposits around obstacles. *J. Sediment. Res.* **64**, 899–909. https://doi.org/10.1306/D4267F00-2B26-11D7-8648000102C1865D (1994).
20. Grue, J. Nonlinear water waves at a submerged obstacle or bottom topography. *J. Fluid Mech.* **244**, 455–476. https://doi.org/10.1017/S0022112092003148 (1992).
21. Lane-Serff, G., Beal, L. & Hadfield, T. Gravity current flow over obstacles. *J. Fluid Mech.* **292**, 39–53. https://doi.org/10.1017/S002211209500142X (1995).
22. Lawrence, G. A. The hydraulics of steady two-layer flow over a fixed obstacle. *J. Fluid Mech.* **254**, 605–633. https://doi.org/10.1017/S0022112093002277 (1993).
23. Muck, M. T. & Underwood, M. B. Upslope flow of turbidity currents: a comparison among field observations, theory, and laboratory models. *Geology* **18**, 54–57. https://doi.org/10.1130/0091-7613(1990)018<0054:UFOTCA>2.3.CO;2 (1990).
24. Ottolenghi, L., Adduce, C., Roman, F. & Armenio, V. Analysis of the flow in gravity currents propagating up a slope. *Ocean Model.* **115**, 1–13. https://doi.org/10.1016/j.ocemod.2017.05.001 (2017).
25. Wilson, R. I., Friedrich, H. & Stevens, C. Turbulent entrainment in sediment-laden flows interacting with an obstacle. *Phys. Fluids* **29**, 036603. https://doi.org/10.1063/1.4979067 (2017).
26. Wilson, R. I., Friedrich, H. & Stevens, C. Flow structure of unconfined turbidity currents interacting with an obstacle. *Environ. Fluid Mech.* **18**, 1571–1594. https://doi.org/10.1007/s10652-018-9631-7 (2018).
27. Wilson, R. I., Friedrich, H. & Stevens, C. Quantifying propagation characteristics of unconfined turbidity currents interacting with an obstacle within the slumping regime. *J. Hydraul. Res.* **57**, 498–516. https://doi.org/10.1046/j.1365-3091.2000.047s1062.x (2019).
28. Woods, A. W., Bursik, M. I. & Kurbatov, A. V. The interaction of ash flows with ridges. *Bull. Volcanol.* **60**, 38–51. https://doi.org/10.1007/s004450050215 (1998).
29. Morris, S. A. & Alexander, J. Changes in flow direction at a point caused by obstacles during passage of a density current. *J. Sediment. Res.* **73**, 621–629. https://doi.org/10.1306/112502730621 (2003).
30. Kubo, Y. S. Experimental and numerical study of topographic effects on deposition from two-dimensional, particle-driven density currents. *Sedim. Geol.* **164**, 311–326 (2004).
31. Khavasi, E., Afshin, H. & Firoozabadi, B. Effect of selected parameters on the depositional behaviour of turbidity currents. *J. Hydraul. Res.* **50**, 60–69. https://doi.org/10.1080/00221686.2011.641763 (2012).
32. Khavasi, E., Firoozabadi, B. & Afshin, H. Linear analysis of the stability of particle-laden stratified shear layers. *Can. J. Phys.* **92**, 103–115. https://doi.org/10.1139/cjp-2013-0028 (2013).
33. Amini, P., Khavasi, E. & Asadizanjani, N. Linear stability analysis of two-way coupled particle-laden density current. *Can. J. Phys.* **95**, 291–296. https://doi.org/10.1139/cjp-2016-0568 (2016).
34. Khavasi, E. & Firoozabadi, B. Linear spatial stability analysis of particle-laden stratified shear layers. *J. Braz. Soc. Mech. Sci. Eng.* **41**, 246. https://doi.org/10.1007/s40430-019-1745-4 (2019).
35. Toniolo, H., Parker, G. & Voller, V. Role of ponded turbidity currents in reservoir trap efficiency. *J. Hydraul. Eng.* **133**, 579–595. https://doi.org/10.1061/(ASCE)0733-9429(2007)133:6(579) (2007).

36. Oehy, C. D. & Schleiss, A. J. Control of turbidity currents in reservoirs by solid and permeable obstacles. *J. Hydraul. Eng.* **133**, 637–648. https://doi.org/10.1061/(ASCE)0733-9429(2007)133:6(637) (2007).
37. Choi, S.-U. & Garcıa, M. H. k-ε turbulence modeling of density currents developing two dimensionally on a slope. *J. Hydraul. Eng.* **128**, 55–63. https://doi.org/10.1061/(ASCE)0733-9429(2002)128:1(55) (2002).
38. Sequeiros, O. E. *et al.* Modeling turbidity currents with nonuniform sediment and reverse buoyancy. *Water Resour. Res.* https://doi.org/10.1029/2008WR007422 (2009).
39. Garcia, M. (American Society of Civil Engineers).
40. Paola, C. & Voller, V. R. A generalized Exner equation for sediment mass balance. *J. Geophys. Res. Earth Surf.* https://doi.org/10.1029/2004JF000274 (2005).
41. Abd El-Gawad, S. *et al.* Three-dimensional numerical simulation of turbidity currents in a submarine channel on the seafloor of the Niger Delta slope. *J. Geophys. Res. Oceans* https://doi.org/10.1029/2011JC007538 (2012).
42. Yeh, T.H., Cantero, M., Cantelli, A., Pirmez, C. & Parker, G,. Turbidity current with a roof: success and failure of RANS modeling for turbidity currents under strongly stratified conditions. *J. Geophys. Res. Earth Surf.* **118**, 1975–1998. https://doi.org/10.1002/jgrf.20126 (2013).
43. Stevens, R. J., Wilczek, M. & Meneveau, C. Large-eddy simulation study of the logarithmic law for second-and higher-order moments in turbulent wall-bounded flow. *J. Fluid Mech.* **757**, 888–907. https://doi.org/10.1017/jfm.2014.510 (2014).
44. Meiburg, E., Radhakrishnan, S. & Nasr-Azadani, M. Modeling gravity and turbidity currents: computational approaches and challenges. *Appl. Mech. Rev.* **67**, 50. https://doi.org/10.1115/1.4031040 (2015).
45. Kundu, P. K. & Cohen, I. M. *Fluid mechanics*. (Elsevier, 2001).
46. Ooi, S., Constantinescu, G. & Weber, L. Numerical simulation of lock-exchange gravity driven flows. *IIHR Technical Rep* **450** (2006).
47. Ooi, S. K., Constantinescu, G. & Weber, L. Numerical simulations of lock-exchange compositional gravity current. *J. Fluid Mech.* **635**, 361–388. https://doi.org/10.1017/S0022112009007599 (2009).
48. Ooi, S. K., Constantinescu, G. & Weber, L. J. 2D large-eddy simulation of lock-exchange gravity current flows at high Grashof numbers. *J. Hydraul. Eng.* **133**, 1037–1047. https://doi.org/10.1061/(ASCE)0733-9429(2007)133:9(1037) (2007).
49. Pelmard, J., Norris, S. & Friedrich, H. LES grid resolution requirements for the modelling of gravity currents. *Comput. Fluids* **174**, 256–270. https://doi.org/10.1016/j.compfluid.2018.08.005 (2018).
50. Pope, S. B. (IOP Publishing, 2001).
51. Mahdinia, M., Firoozabadi, B., Farshchi, M., Varnamkhasti, A. G. & Afshin, H. Large eddy simulation of Lock-Exchange flow in a curved channel. *J. Hydraul. Eng.* **138**, 57–70. https://doi.org/10.1061/(ASCE)HY.1943-7900.0000482 (2012).
52. Nasr-Azadani, M. & Meiburg, E. Turbidity currents interacting with three-dimensional seafloor topography. *J. Fluid Mech.* **745**, 409–443. https://doi.org/10.1017/jfm.2014.47 (2014).
53. Nasr-Azadani, M. M. & Meiburg, E. TURBINS: an immersed boundary, Navier-Stokes code for the simulation of gravity and turbidity currents interacting with complex topographies. *Comput. Fluids* **45**, 14–28. https://doi.org/10.1016/j.compfluid.2010.11.023 (2011).
54. Bonometti, T. & Balachandar, S. Effect of Schmidt number on the structure and propagation of density currents. *Theoret. Comput. Fluid Dyn.* **22**, 341. https://doi.org/10.1007/s00162-008-0085-2 (2008).
55. Nasr-Azadani, M. M., Meiburg, E. & Kneller, B. Mixing dynamics of turbidity currents interacting with complex seafloor topography. *Environ. Fluid Mech.* **18**, 201–223. https://doi.org/10.1007/s10652-016-9477-9 (2018).
56. Dietrich, W. E. Settling velocity of natural particles. *Water Resour. Res.* **18**, 1615–1626. https://doi.org/10.1029/WR018i006p01615 (1982).
57. Nasr-Azadani, M., Hall, B. & Meiburg, E. Polydisperse turbidity currents propagating over complex topography: comparison of experimental and depth-resolved simulation results. *Comput. Geosci.* **53**, 141–153. https://doi.org/10.1016/j.cageo.2011.08.030 (2013).
58. Smagorinsky, J. General circulation experiments with the primitive equations: I. The basic experiment. *Mon. Weather Rev.* **91**, 99–164. https://doi.org/10.1175/1520-0493(1963)091%3C0099:GCEWTP%3E2.3.CO;2 (1963).
59. Goodarzi, D., Lari, K. S. & Alighardashi, A. A large eddy simulation study to assess low-speed wind and baffle orientation effects in a water treatment sedimentation basin. *Water Sci. Technol.* **412–421**, 2018. https://doi.org/10.2166/wst.2018.171 (2017).
60. Lari, K. S., van Reeuwijk, M. & Maksimović, Č. The role of geometry in rough wall turbulent mass transfer. *Heat Mass Transf.* **49**, 1191–1203. https://doi.org/10.1007/s00231-013-1194-z (2013).
61. Farizan, A., Yaghoubi, S., Firoozabadi, B. & Afshin, H. Effect of an obstacle on the depositional behaviour of turbidity currents. *J. Hydraul. Res.* **57**, 75–89. https://doi.org/10.1080/00221686.2018.1459891 (2019).
62. Choi, H. & Moin, P. Grid-point requirements for large eddy simulation: Chapman's estimates revisited. *Phys. Fluids* **24**, 011702. https://doi.org/10.1063/1.3676783 (2012).
63. Chapman, D. R. Computational aerodynamics development and outlook. *AIAA journal* **17**, 1293–1313. https://doi.org/10.2514/3.61311 (1979).
64. Wylie, E. B. & Streeter, V. L. Fluid transients. *New York, McGraw-Hill International Book Co., 1978. 401 p.* (1978).
65. Ferziger, J. H., Perić, M. & Street, R. L. *Computational methods for fluid dynamics*. Vol. 3 (Springer, 2002).
66. Jasak, H. Error analysis and estimation for the finite volume method with applications to fluid flows. (1996).
67. Issa, R. I. Solution of the implicitly discretised fluid flow equations by operator-splitting. *J. Comput. Phys.* **62**, 40–65. https://doi.org/10.1016/0021-9991(86)90099-9 (1986).
68. Oehy, C. D., De Cesare, G. & Schleiss, A. J. Effect of inclined jet screen on turbidity current. *J. Hydraul. Res.* **48**, 81–90. https://doi.org/10.1080/00221680903566042 (2010).
69. Nourazar, S. & Safavi, M. Two-dimensional large-eddy simulation of density-current flow propagating up a slope. *J. Hydraul. Eng.* **143**, 04017035. https://doi.org/10.1061/(ASCE)HY.1943-7900.0001329 (2017).
70. Goodarzi, D., Abolfathi, S. & Borzooei, S. Modelling solute transport in water disinfection systems: Effects of temperature gradient on the hydraulic and disinfection efficiency of serpentine chlorine contact tanks. *J. Water Process Eng.* **37**, 101411. https://doi.org/10.1016/j.jwpe.2020.101411 (2020).
71. Dong, S., Salauddin, M., Abolfathi, S., Tan, Z. H. & Pearson, J. M. The influence of geometrical shape changes on wave overtopping: a laboratory and SPH numerical study. In *Coasts, Marine Structures and Breakwaters 2017* 1217–1226. https://doi.org/10.1680/cmsb.63174.1217 (2018).
72. Fitri, A., Hashim, R., Abolfathi, S. & Abdul Maulud, K. N. Dynamics of sediment transport and erosion-deposition patterns in the locality of a detached low-crested breakwater on a cohesive coast. *Water* **11**, 1721. https://doi.org/10.3390/w11081721 (2019).
73. Abolfathi, S., Shudi, D., Borzooei, S., Yeganeh-Bakhtiari, A. & Pearson, J. Application of smoothed particle hydrodynamics in evaluating the performance of coastal retrofit structures. *Coast. Eng. Proc.* **1**. https://doi.org/10.9753/icce.v36.papers.109 (2018).
74. Abolfathi, S. & Pearson, J. Application of smoothed particle hydrodynamics (SPH) in nearshore mixing: a comparison to laboratory data. *Coast. Eng. Proc.* **1**. https://doi.org/10.9753/icce.v35.currents.16 (2017).
75. Wood, I. & Simpson, J. Jumps in layered miscible fluids. *J. Fluid Mech.* **140**, 329–342. https://doi.org/10.1017/S0022112084000628 (1984).
76. Kneller, B. & Buckee, C. The structure and fluid mechanics of turbidity currents: a review of some recent studies and their geological implications. *Sedimentology* **47**, 62–94. https://doi.org/10.1046/j.1365-3091.2000.047s1062.x (2000).

### Author contributions

D.G., S.A. and K.S.L. wrote the manuscript. D. Goodarzi generated all the simulation figures. D.G. and E.K. developed the CFD model and conducted parallel computations. All the authors participated in data analysis, discussion and results preparation. The manuscript was reviewed by all authors.

### Competing interests

The authors declare no competing interests.

### Additional information

**Correspondence** and requests for materials should be addressed to D.G.

**Reprints and permissions information** is available at www.nature.com/reprints.

**Publisher's note** Springer Nature remains neutral with regard to jurisdictional claims in published maps and institutional affiliations.